

# A study of the T. Mayer B lunar highland dome

Rodrigo Viegas, Raffaello Lena, Christian Wöhler & Jim Phillips

This study describes a highland dome that to our knowledge was previously unreported; it is neither on the ALPO list nor classified. Positioned at  $31^{\circ}.08\text{W}$  and  $14^{\circ}.77\text{N}$  ( $\xi = -0.4992, \eta = 0.2549$ ), this dome stands about 100km to the NW of the well known highland dome adjacent to T. Mayer D, embedded in the hummocky terrain south of the Carpathian Mts. We report CCD imagery including a calculated slope and height for the dome. An image-based three-dimensional reconstruction of the dome is performed based on a shape-from-shading approach. This has made it possible to extract additional information for its classification and interpretation in geological terms.

## 1. Introduction

Lunar domes are gentle swells between 3 and 60km across and, at most, a few hundred metres high, similar to the low shield volcanoes found on Earth.<sup>1,2</sup> They represent the terminal phase of lunar volcanism and they occur mostly in the maria. Most have very low angles of inclination, not more than a few degrees. Many have a central ‘crater pit’, which occurs upon magma withdrawal with collapse around the vent. Domes also occur in the highlands, but are usually difficult to see because of the brightness and ruggedness of the region.<sup>3</sup>

The Hortensius–Milichius–T. Mayer region is possibly one of the most thoroughly studied by dome observers; in it more than 40 domes have been reported.<sup>4–5</sup> Nevertheless, the only highland dome reported in this region is the one adjacent to T. Mayer D.<sup>6</sup> In this study we describe a highland dome adjacent to T. Mayer B, which does not appear in the ALPO Lunar Dome Survey database or in the updated list of highland domes given in references 6 & 7.

## 2. Highland domes

The term ‘highland domes’ refers to domes of a higher albedo than the mare regions; they are positioned in the highland regions. Highland domes are usually difficult to discern because of the brightness and ruggedness that characterises the surrounding highland materials.

As to their geology, there are two theories. The first argues that the higher reflectance of these domes suggests that they have a different mineralogy, and this is most consistent with lava having a lower iron and titanium content.<sup>6,9</sup> This theory is in agreement with the majority of highland

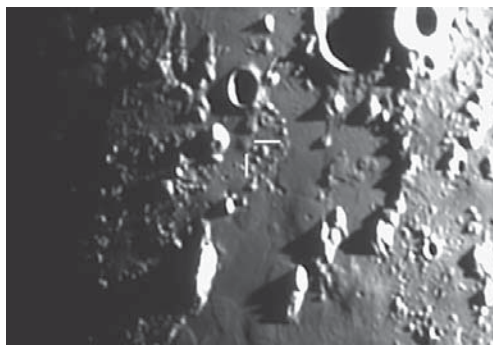


**Figure 1.** The dome under morning illumination. 2004 December 22, 02:37 UT, TMB 203mm f/9 apochromatic refractor, Atik b/w camera (Alt.  $2^{\circ}.65$ , Col.  $34^{\circ}.29$ ). Jim Phillips.

domes being steep, because low iron and titanium lavas are more viscous and thus can be expected to pile up more easily, producing steeper constructs. The classical example of highland domes is Gruithuisen Gamma which has a higher albedo than the nearby Mare Imbrium, and also a steeper slope than mare domes. This refers to ‘an early volcanism which was both unrelated to the physical maria and was also of different mineralogy’.<sup>3</sup> A second theory argues that highland domes are covered by a thin veneer of ejecta from the Imbrium impact.<sup>6</sup>

The different mineralogy considered in the first theory would imply higher slopes, and this may account for the fact that more than fifty percent of the reported highland domes have moderate slopes ( $2\text{--}5^{\circ}$ ). Nevertheless, it has to be noted that highland domes tend to appear as steeper features than they really are, even to the trained observer. This ‘optical effect’ may be due to the fact that highland domes have a higher albedo than mare domes. This makes the contrast between the shadow and the summit much stronger in the case of highland domes than for mare domes. Consequently, the observer is misled into an exaggerated evaluation of the highland dome slope. In another recent paper,<sup>8</sup> some of us reported a study of the Piccolomini highland dome, which revealed a slope of only  $1^{\circ}.7$ .

## 3. Instruments and measurements

From our available images (Figures 1–3) and using the Lunar Aeronautical Chart (LAC) #57, it was possible to determine the dome position as  $31^{\circ}.08\text{W}$  and  $14^{\circ}.77\text{N}$  ( $\xi = -0.4992, \eta = 0.2549$ ). For each of the observations, the solar altitude on the dome (Alt.) and the Sun’s selenographic colongitude (Col.) were calculated using the *Lunar Observer’s Toolkit* by H. D. Jamieson (ALPO).<sup>13</sup> Moreover, the corresponding scale of the images was obtained, allowing the dome diameter to be expressed in



**Figure 2.** 2005 January 20, 18:43 UT, 305mm SCT, Vesta Pro webcam (Alt. 3°.33, Col. 34°.93). *Alessandro Bianconi.*



**Figure 3.** 2005 January 20, 20:59 UT, 235mm SCT (Alt. 4°.44, Col. 36°.08). *Rafael Benavides.*

kilometres. All the images are oriented with north upwards and west (IAU) to the left.

Our data are consistent with the measurements obtained using a high-resolution version of the Lunar Orbiter frame IV-133-H2,<sup>15</sup> here presented as Figure 5. A 3D

reconstruction was performed using the images shown in Figures 1 and 2, taken with an Atik B&W and a Vesta Pro webcam, respectively. A gamma calibration was carried out for these images (cf. Section 3.3). Tables 1 and 2 summarise the measurements.

### 3.1. Vertical cross-section

Information about the vertical cross-section was obtained using the Ashbrook method.<sup>16</sup> Using this method, we estimated the fraction  $x$  of the dome's east-west diameter that is covered by black shadow. According to Ashbrook the average slope of the dome flank is equal to the solar altitude for  $x = 0.25$ , under the assumption that the dome is of hemispherical shape, which is realistic for most regular domes. The height  $H$  of the dome was then calculated by

$$H = r (\tan s) \quad [1]$$

**Table 1. Measurements of the high-resolution image LO-IV-133-H2**

Position		E-W dome diameter ( $W_{do}$ )		Diameter of summit crater ( $W_{cr}$ )	
Long. (°)	Lat. (°)	pixels	Km	pixels	Km
31.08W	14.77N	92±1	6.0±0.3	15±1	1.0±0.3

**Table 2. Height measurements of the dome located at 31°.08W and 14°.77N in Figures 1 & 2, obtained using the Ashbrook method.<sup>16</sup>**

Data	Solar alt. (°)	Dome diameter		Shadow length		Height (m)	Slope (°)
		pixels	Km	pixels	Km		
Fig.1	2.65	20±1	6.0±0.3	5±1	1.5±0.3	140±14	2.7
Fig.2	3.33	19±1	5.7±0.3	5±1	1.5±0.3	160±24	3.2

where  $r$  is the radius of the dome and  $(\tan s)$  is the tangent of the average slope angle when the dome is one quarter covered by black shadow. The results are reported in Table 2.

### 3.2. Morphometric characteristics

Morphometric relations were obtained using the dome basal diameter ( $W_{do}$ ) and crater diameter ( $W_{cr}$ ) as proposed by Wood.<sup>14</sup> The horizontal dimensions ( $W_{do}$  and  $W_{cr}$ ) distinguish pyroclastic cones from lava shields. Plotting  $W_{cr}/W_{do}$  versus  $W_{do}$ , Wood defined the morphological types as C (cinder cones), SS (steep shield volcano), SL (low shield volcano) and SI (icelandic shield). Moreover, the dome was classified using the Head & Gifford scheme<sup>12</sup> and the Westfall classification scheme.<sup>11</sup> The height–base diameter relationship was also determined, plotting our data on Head & Gifford's diagram.<sup>12</sup>

### 3.3. 3D reconstruction of the highland dome by photoclinometry and shape-from-shading

We have generated an elevation map of the highland dome near Tobias Mayer based on our telescopic CCD images, utilising a method based on photoclinometry and shape-from-shading (SFS). A general outline of this method is given in our earlier paper.<sup>17</sup> The SFS technique aims at deriving the orientation of the surface at each image location by using a model of the reflectance properties of the surface and knowledge about the illumination conditions, finally leading to an elevation value for each image pixel.<sup>18</sup> In this paper we employ a refined approach based on two subsequent reconstruction steps and an accurate reflectance function.

Our first processing step was a gamma calibration of our CCD images as previously described,<sup>17</sup> leading to a linear dependency between pixel greyvalue and light intensity. The shape-from-shading method requires accurate knowl-

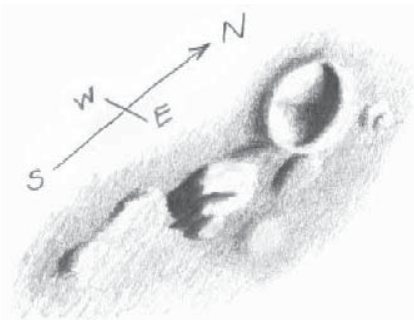


**Figure 4.** Visual observation on 2005 January 21, 00:35–01:25 UT. 114mm f/7.9 Newtonian ×140 (Alt. at 01:00 6°.40, Col. 38°.10). *Rodrigo Viegas.*

edge of the scattering properties of the surface. An appropriate relation is the physically motivated photometric model by Hapke,<sup>19</sup> which is based on the theory of radiative transfer. It depends on certain surface properties such as the average particle size, the particle density, the albedo of the surface material, or the macroscopic surface roughness. Sets of Hapke parameters valid for the lunar regolith are given e.g. by Warell.<sup>20</sup> As it is not straightforward, however, to directly employ the Hapke model for 3D reconstruction purposes, in many astrogeological applications the empirical Lunar–Lambert law is used:

$$R_{LL}(\rho, \theta_i, \theta_e, \alpha) = \rho [2 L(\alpha) \cos \theta_i / (\cos \theta_i + \cos \theta_e) + (1 - L(\alpha)) \cos \theta_i]$$

with  $\rho$  as the surface albedo,  $\theta_i$  as the angle between surface normal and illumination direction,  $\theta_e$  as the angle between surface normal and viewing direction, and the Lunar–Lambert parameter  $L(\alpha)$  as an empirical value depending on the phase angle  $\alpha$ . Given a suitable choice of  $L(\alpha)$ , the Lunar–Lambert law fits the true scattering behaviour of a planetary surface equally as well as the Hapke model. Values for  $L(\alpha)$  have been tabulated in McEwen<sup>21</sup> for planetary surfaces with a wide range of regolith properties. The CCD images presented in this paper have been acquired under phase angles around  $60^\circ$ . In this case, McEwen yields  $L(\alpha) = 0.8$  for a surface with the Hapke parameters of the lunar regolith, according to Warell.<sup>20</sup>

We will assume that the scene is illuminated exactly along the image rows, which are oriented in an east–west direction. The surface normal at a pixel position  $(u,v)$  is given by the slopes  $p(u,v)$  in an east–west direction and  $q(u,v)$  in a north–south direction.

In a first step we follow the approach of *photoclinometry*, which consists of computing height profiles along image rows. It can be shown that for gently sloping terrain ( $p, q \ll 1$ ) and oblique illumination, the surface reflectance  $R_{LL}$  depends much more strongly on  $p$  than on  $q$ . We thus assume  $q = 0$  and then compute  $p$  individually for each pixel by setting the observed pixel intensity  $I_{obs}$  equal to the modelled reflectance, respectively:

$$I_{obs}(u,v) = R_{LL}(u,v)$$

The uniform surface albedo  $\rho$  is estimated based on the realistic assumption of a surface whose eastern border is on the same height level as its western border, *i.e.* for which the average value of  $p$  is zero. In this manner, a slope  $p(u,v)$  in the east–west direction can be obtained for each pixel  $(u,v)$  in the image. A height value relative to the image border can then be derived for each pixel by summing up the slope values along the image row (*cf.* the upper row of Figure 6).

In a second step, the SFS algorithm adjusts for each pixel position  $(u,v)$  the slopes  $p(u,v)$  (east–west direction) and  $q(u,v)$  (north–south direction) of the model surface such that the resulting mean square deviation,  $[I_{obs}(u,v) - R_{LL}(u,v)]^2$ , between the observed and modelled intensity of reflected light is minimised. The height profile  $z(u,v)$  is obtained by integration of the surface slopes. According to section 5.1 of Horn,<sup>18</sup> we employ an iterative scheme for the surface slopes  $p(u,v)$  and  $q(u,v)$  and the height  $z(u,v)$ , which consists of the following steps:

- 1 For each pixel  $(u,v)$ , set the initial values for  $p(u,v)$  according to the results of the photoclinometric procedure described above, and set the initial values for  $q(u,v)$  to zero.
- 2 Compute the albedo  $\rho$  based on the current values of the surface slopes.
- 3 For each pixel  $(u,v)$  update the surface slopes  $p(u,v)$  and  $q(u,v)$  by a small amount such that  $[I_{obs}(u,v) - R_{LL}(u,v)]^2$  is reduced.

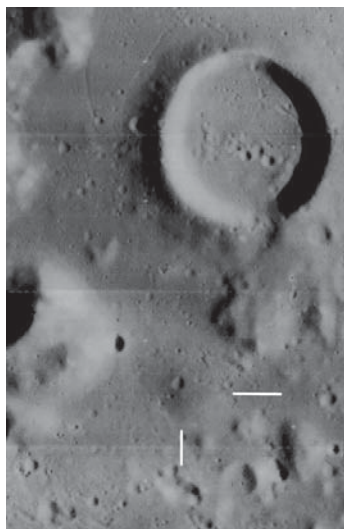


Figure 5. Lunar Orbiter frame IV-133-H2, displayed in high resolution.<sup>15</sup>

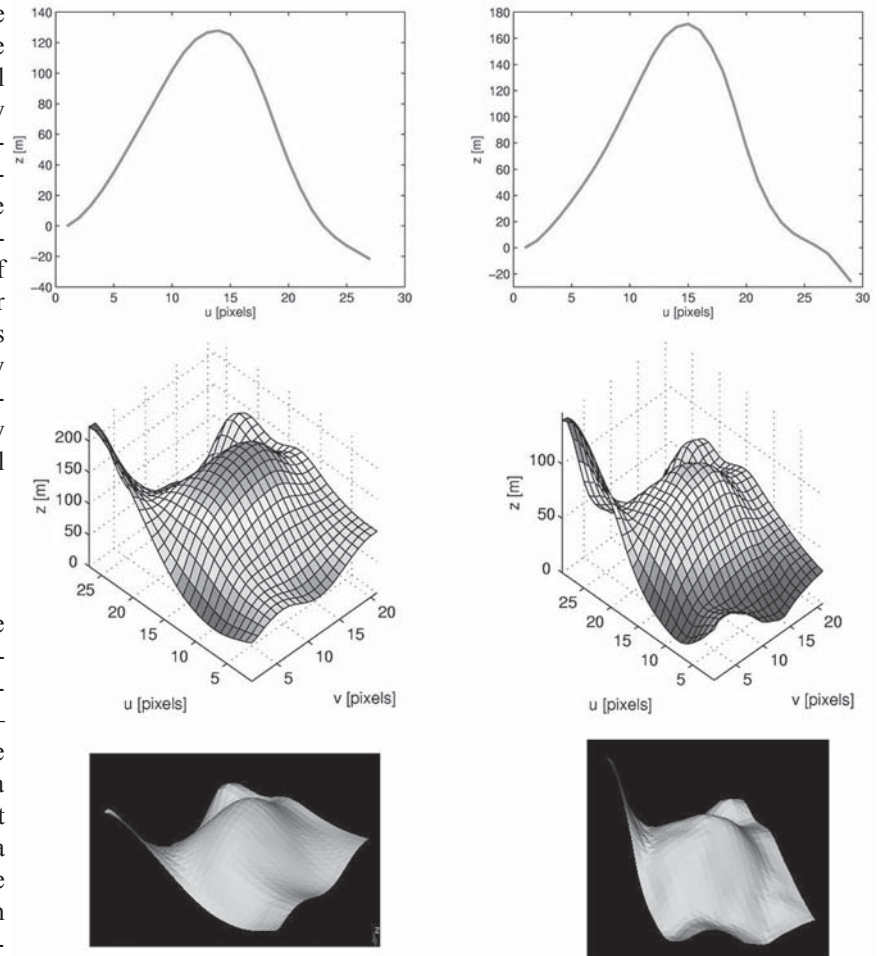


Figure 6. 3D reconstruction results; see text.

- 4 Update the height  $z(u,v)$  according to the new slope values.
- 5 Repeat steps 2–4 until the average deviation  $[I_{\text{obs}}(u,v) - R_{\text{LL}}(u,v)]^2$  does not decrease any more.

In the original version of the algorithm as described in Horn,<sup>18</sup> all initial surface slopes  $p(u,v)$  and  $q(u,v)$  are set to zero. The algorithm, however, then tends to underestimate the height of objects, especially of small ones like the highland dome considered in this study. We have therefore initialised the east-western slopes  $p(u,v)$  according to the photogrammetric procedure described above, which yields a much better correspondence between observed and modelled intensity distributions.

## 4. Observations and digital images

Figure 1 displays the dome under a morning illumination. This image was taken by Jim Phillips on 2004 December 22 at 02:37 UT using a 203mm f/9 apochromatic refractor.

On 2005 January 20, the dome was imaged by Alessandro Bianconi (Italy) at 18:43 UT and Rafael Benavides (Spain) at 20:59 UT (Figures 2 and 3, respectively). Some hours later, on 2005 January 21 between 00:35 and 01:25 UT, Viegas carried out a visual observation (Figure 4). The drawing was made using a 114mm Newtonian at  $f/7.9 \times 140$ .

This dome is visible on frames D20, D21 and D23 of the *Consolidated Lunar Atlas*.<sup>22</sup> It is of note that none of the Earth-based observations reveals any summit detail, except a very subtle structure visible in the rendered view of the dome derived from Figure 2, shown in Figure 6 (lower right). In contrast, frame LO-IV-133 H2 (Figure 5) clearly shows a summit crater pit estimated as 1 km in diameter (Table 1).

## 5. Results and discussion

This dome requires a specific solar altitude for it to be observed clearly. The height of the dome was then estimated using Equation (1) for Figures 1 and 2. It turns out that the summit of the dome is 140m higher than the surrounding plain using the image in Figure 1 and 160m higher using the image in Figure 2. Most probably, the uncertainty in the dome height is related to the difficulty in distinguishing between umbra and penumbra for small shadows. The height measurements, however, are consistent which each other due to the fact that their error intervals overlap.

From Table 2 it follows that the maximum slope angle of the dome is  $<5^\circ$ , corresponding to a hemispherical circular dome having a moderate slope. Moreover, a crater/pit on the dome summit was detected on frame IV-133-H2. From Table 1 it follows that the dome has a base diameter of  $(6.0 \pm 0.3)$ km with a crater pit of  $(1.0 \pm 0.3)$ km diameter.

Figure 6 shows the 3D reconstruction results obtained by means of the shape-from-shading method described in detail in Section 3.3 for the images in Figure 1 (left column) and Figure 2 (right column). Each column displays a cross-section through the summit of the dome obtained with the photogrammetric approach (top), the result of 3D reconstruction viewed from the northwest (middle), and a rendered view derived from the computed 3D structure of the dome (bottom, vertical axis 20 times exaggerated). Image scale is 296m/pixel for Figure 1 and 303m/pixel for Figure 2. The effective dome height obtained by 3D reconstruction is  $(135 \pm 20)$ m for the image in Figure 1 and  $(160 \pm 20)$ m for the image in Figure 2, corresponding to an average slope of  $2^\circ.5 \pm 0^\circ.4$  and  $3^\circ.1 \pm 0^\circ.4$ , respectively. These values are in good agreement with those obtained by means of the Ashbrook method<sup>16</sup> given in Table 2. The main reason for the (moderate) discrepancy between the two height values is the non-zero brightness of the small shadow of the dome in Figure 1, which may be caused by light scattered inside the telescope optics, leading to an underestimation of the effective dome height. The rendered view derived from Figure 2 (right column, bottom image) reveals a structure situated slightly off the dome summit that might correspond to the summit crater pit visible in the *Lunar Orbiter* image in Figure 5.

As a note of interest, the relationship between height and base diameter for the dome (see Figure 7) matches the terrestrial example of the Icelandic type in the diagram published in Head & Gifford.<sup>12</sup> However, even if the morphometric quantities of the dome are consistent with Icelandic shields, this does not prove that this dome is a shield and has been formed by similar mechanisms. Differences between terrestrial and lunar structures make the comparison uncertain because the physical processes involved are probably very different.

A comparison of the geometry of extraterrestrial cones and domes as described by Wood<sup>20</sup> shows that the structure overlaps significantly in the lava shields signature (see Figure 8).

With our data, we can establish a generic classification for this dome, using both the Westfall<sup>11</sup> and the Head & Gifford<sup>12</sup> classification schemes. It can be categorised as DU/2a/6f/7j using the Westfall scheme and as of Class 1 using the Head & Gifford classification. Class 1 domes have circular or elliptical outlines, a summit crater and slopes under  $5^\circ$ ; they merge smoothly with the surrounding terrain, as is the case here.

## 6. Geological considerations

This dome is positioned about 80km outside the third and outermost of the rings that once constituted the impressive Imbrian basin. Close inspection of the IV-133-H2 frame (Figure 5) reveals that the summit crater has an oval shape and shows no rim; moreover, it appears to be formed by two overlapped craterlets, which likely represent the central volcanic vents. It is very interesting to note that the dome appears covered by dark soils, which can be interpreted as ash deposits.

The presence of another highland dome about 100km to the SE cannot be ignored; this feature also exhibits a summit craterlet, as is seen on Figure 3. This well-known highland dome is classified as Eratosthenian mare dome material (Emd).<sup>10</sup> Interestingly, the dome we are dealing with does not appear as an identified feature in the classification, possibly due to its small size; instead, it is included as part of an Em unit (Eratosthenian mare material). Em is described as 'Probably relatively thin cover of young flows or pyroclastic materials over thicker accumulations of Imbrian mare material'.<sup>10</sup> A possible interpretation is that this dome is in fact an Emd partially eroded by meteoritic bombardment.

## 7. Conclusion

The highland dome at 31°.08W and 14°.77N is a further clear example of the elusive nature of highland domes. This study shows that a combination of careful visual and CCD observations made by different observers provides powerful tools for the study and interpretation of lunar domes. Moreover, it also shows that in the case of highland domes special attention should be paid when assessing their slopes.

## Acknowledgments

We wish to thank Alessandro Bianconi and Rafael Benavides for their contribution to this paper.

**Address:** Geologic Lunar Research Group (GLR), Via Cartesio 144, 00137 Rome, Italy. [lena@glrgroup.org]

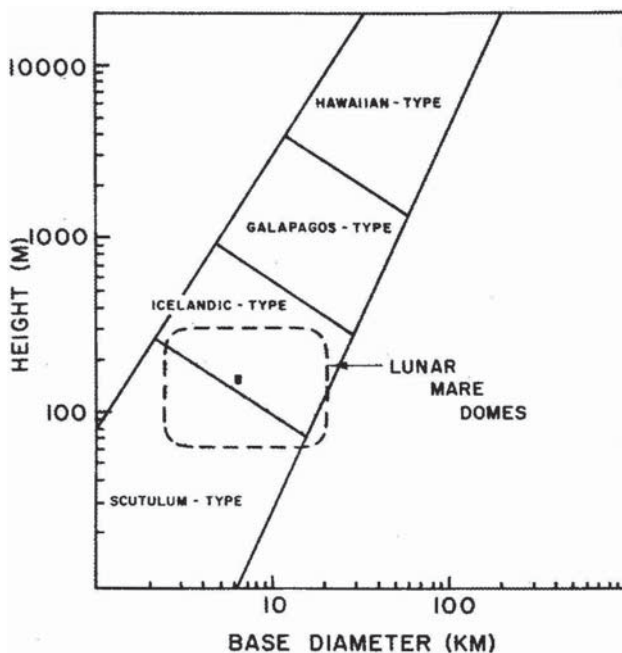


**Figure 7.** The relationship between height and base diameter for the dome matches the terrestrial example of the Icelandic type in Head & Gifford.<sup>12</sup>

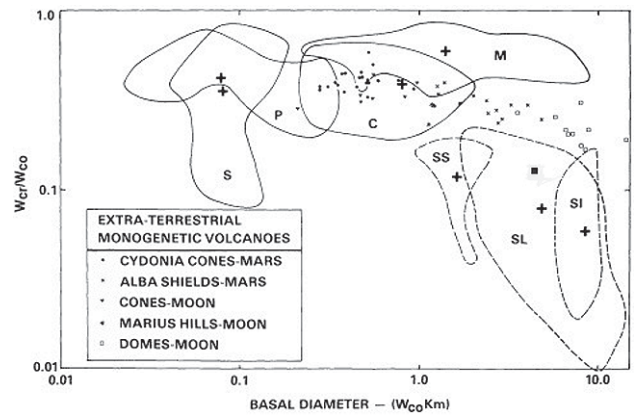


**Figure 8.** A comparison of the geometry of extraterrestrial cones and domes as described by Wood.<sup>20</sup>

## References

- 1 Wilhelms D., *The Geologic History of the Moon*, USGS Prof. Paper 1348, Washington: GPO, 1987
- 2 Salimbeni P. et al., 'The three domes in Rima Birt region', *JALPO*, **42**(2), 83–87 (2000)
- 3 Viegas R. et al., 'Piccolomini highland dome', *Selenology*, **21**(2), 15–18 (2002)
- 4 Phillips J., 'The New Lunar Dome Survey: the Hortensius-Milichius-Tobias Mayer region', *JALPO*, **33**(4–6), 61–72 (1989)
- 5 Phillips J., 'Observations of lunar domes north-northwest of Milichius: an interpretation', *JALPO*, **33**(4–6), 73–74 (1989)
- 6 Douglass E. & Santacana G., 'Highland domes and a highland dome near Zollner', *Selenology*, **21**(2), 8–12 (2002)
- 7 Viegas R. et al., 'Highland dome near T. Mayer-B and two cones near Milichius', *The Lunar Observer*, 2005 February, pp. 4–5
- 8 Lena R. et al., 'A generic classification of the dome near Piccolomini', *JALPO*, **45**(3), 22–27 (2003)
- 9 Spudis P., 'Volcanism on the Moon', in Sigurdsson H. (ed.), *Encyclopedia of Volcanoes*, Academic Press, San Diego, 2000, p. 705
- 10 Wenker A., *Geologic map of the near side of the Moon*, US Geological Survey, Flagstaff, 1999
- 11 Westfall J., 'A generic classification of lunar domes', *JALPO*, **18**(1–2), 15–20 (1964)
- 12 Head J. W. & Gifford A., 'Lunar domes: Classification and modes of origin', *Moon and Planets*, **22**, 235–258 (1980)
- 13 Jamieson H. D., 'The Lunar Dome Survey – Fall 1992 progress report', *Strolling Astronomer*, **37**(1), 14–17 (1993)
- 14 Wood C. A., 'Monogenetic volcanoes of the terrestrial planets', *Proc. 10th Lunar Planet. Sci. Conf.*, 2815–2840 (1979)
- 15 <http://astrogeology.usgs.gov/>
- 16 Ashbrook J., *JALPO*, **15**(1–2), 1–3 (1961)
- 17 Lena R. et al., 'Lunar domes: a generic classification of the dome near Valentine located at 10.26°E and 31.89°N', *J. Brit. Astron. Assoc.*, **116**(1), 34–39 (2006)
- 18 Horn B. K. P., *Height and gradient from shading*, MIT technical report, AI memo no. 1105A, 1989. <http://people.csail.mit.edu/people/bkph/AIM/AIM-1105A-TEX.pdf>
- 19 Hapke B., *Theory of reflectance and emittance spectroscopy*, Cambridge University Press, 1993
- 20 Warell J., 'Properties of the Hermean regolith: IV. Photometric parameters of Mercury and the Moon contrasted with Hapke modelling', *Icarus*, **167**(2), 271–286 (2004)
- 21 McEwen A. S., 'Photometric functions for photoclinometry and other applications', *Icarus*, **92**, 298–311 (1991)
- 22 Kuiper G. P. et al., *Consolidated Lunar Atlas*, Lunar & Planetary Laboratory, Univ. Arizona, 1967. Digital version by E. Douglass, <http://www.lpi.usra.edu/resources/cla/>

Received 2005 April 12; accepted 2005 September 7